Tunable genetic devices through simultaneous control of transcription and translation

Vittorio Bartoli[1,2], Grace A. Meaker[3], Mario di Bernardo[1,2,4] and Thomas E. Gorochowski[1,5,*]

[1] BrisSynBio, University of Bristol, Life Sciences Building, Tyndall Avenue, Bristol, UK
[2] Department of Engineering Mathematics, University of Bristol, Woodland Road, Bristol, UK
[3] School of Biosciences, Cardiff University, Museum Avenue, Cardiff, UK
[4] Department of Electrical Engineering and Information Technology, University of Naples Federico II, Via Claudio 21, Napoli, Italy
[5] School of Biological Sciences, University of Bristol, Bristol, Tyndall Avenue, UK

* Correspondence should be addressed to T.E.G. (thomas.gorochowski@bristol.ac.uk)

Keywords: gene regulation; genetic circuits; transcription; translation; toehold switch; synthetic biology; systems biology.

Abstract

Synthetic genetic circuits allow us to modify the behavior of living cells. However, changes in environmental conditions and unforeseen interactions between a circuit and the host cell can cause deviations from a desired function, resulting in the need for time-consuming physical re-assembly to fix these issues. Here, we use a regulatory motif that controls transcription and translation to create genetic devices whose response functions can be dynamically tuned. This approach allows us, after construction, to shift the ‘on’ and ‘off’ states of a sensor by 4.5- and 28-fold, respectively, and modify genetic NOT and NOR logic gates to allow their transitions from an ‘on’ to ‘off’ state to be varied over a >6-fold range. In all cases, tuning leads to trade-offs in the fold-change and separation between the distributions of cells in ‘on’ and ‘off’ states. By using mathematical modelling, we derive design principles that help to further optimize the performance of these devices. This work lays the foundation for adaptive genetic circuits that can be tuned after their physical assembly to maintain functionality across diverse environments and design contexts.

Introduction

Gene regulatory networks, or genetic circuits as they are often known, govern when and where genes are expressed in cells and control core biochemical processes like transcription and translation [1,2]. The ability to synthesize DNA encoding engineered genetic circuits offers a means to expand the capabilities of a cell and reprogram its behavior [1,3]. Synthetic genetic circuits have been built to implement computational operations [4–12], dynamic behaviors like oscillations [13–15], and even coordinate multicellular actions across a population [16–20].

The ability to reprogram living cells is simplified by using genetically encoded devices that use common input and output signals [1,2,7,9]. This allows the output of one device to be directly connected to the input of another to create circuits implementing more complex functionalities. Signals can take many forms, but one of the most commonly used is RNA polymerase (RNAP) flux in which promoters are used to guide this signal to specific points in a circuit's DNA [7,21]. Based on such input and output signals, the response function of a genetic device captures how inputs map to outputs at steady state [1,7,21]. By ensuring the response functions of two devices are compatible, i.e. they are "matched" such that the range of the output of the first device spans the necessary range of inputs for the second device, larger circuits with desired functions can be constructed [22]. Matching of components is vital in circuits where devices exhibit switching behaviors (e.g. for Boolean logic) to ensure input signals are sufficiently separated to accurately trigger required transitions between 'on' and 'off' states as signals propagate through the circuit.

Although the use of characterized genetic devices has enabled the automated design of large genetic circuits [7,23], the response functions of these devices are often sensitive to many factors. For example, differences in host physiology due to culturing conditions [24–26] and interactions between genetic parts and the host cell [27–32], can all affect the response function of a device and subsequently its compatibility within a circuit. This makes the creation of reliable and robust genetic circuits a challenge. Even when considering carefully controlled conditions, like those in the lab, a genetic circuit often needs to be reassembled from scratch multiple times using alternative parts until a working combination is found. This is both time consuming and expensive, and often has to be repeated if the circuit is to be deployed in slightly different conditions or host strains.

In this work, we tackle this problem by developing genetic devices whose response functions can be dynamically tuned after physical assembly to correct for unwanted changes in their behavior. The ability to tune/modify the steady state input-output relationship is made possible by employing a simple regulatory motif. We show how this motif can be connected to small molecule sensors to characterize its function and then illustrate how it can be used in practice by integrating it into genetic NOT and NOR logic gates [33] to allow for the tuning of the

transition point between 'on' and 'off' states. These capabilities make these devices more broadly compatible with other components [1,7,22], but their use comes at a cost because of trade-offs in their performance. As we tune the devices, a decrease in the dynamic range is observed and the ability to differentiate 'on' and 'off' states due to variability in gene expression across a population. We use mathematical modelling to better understand these limitations and derive design principles that are then used to further optimize their design. This work is a step towards genetic circuitry whose individual components can functionally adapt, ensuring robust system-level behaviors are maintained no matter the genetic, cellular or environmental context.

Results

Controlling transcription and translation using a tunable expression system

To allow for the response of a genetic device to be modulated, we developed a tunable expression system (TES) based on a simple regulatory motif where two separate promoters control the transcription and translation rates of a gene of interest (**Figure 1a**). By using promoters as inputs, it is possible to easily connect a TES to existing genetic components/circuitry or even endogenous transcriptional signals within a cell. The TES consists of a toehold switch (THS) that enables the translation initiation rate of the gene of interest to be varied by the relative concentration of a "tuner" small RNA (sRNA) [6,34]. The main component of the THS is a 92 bp DNA sequence that encodes a structural region and a ribosome binding site (RBS) used to drive translation of a downstream protein coding region. This is expressed from a promoter that acts as the main input to the TES (**Figure 1a**). When transcribed, the structural region of the THS mRNA folds to form a hairpin loop secondary structure that makes the RBS less accessible to ribosomes and thus reduces its translation initiation rate. This structure is disrupted by a second component, a 65 nt tuner sRNA that is complementary to the first 30 nt of the THS [34]. The tuner sRNA is expressed from a second promoter, which acts as a tuner input to the device (**Figure 1a**). Complementarity between the tuner sRNA and a short unstructured region of the toehold switch enables initial binding, which then makes it thermodynamically favorable for the sRNA to unfold the secondary structure of the THS through a branch migration process. This makes the RBS more accessible to ribosomes which increases the translation initiation rate. Relative concentrations of the THS mRNA and tuner sRNA (controlled by the input and tuner promoters) enable the rate of translation initiation to be potentially varied over a 100-fold range for the toehold switch design we selected for our own [34] (**Materials and Methods**). However, THS designs exist which allow for up to a 400-fold change in translation initiation rates [6,34].

We selected as main and tuner inputs for the TES the output promoters of two sensors, P_{tet} and P_{tac}, that respond to anhydrotetracycline (aTc) and isopropyl β-D-1-thiogalactopyranoside (IPTG), respectively (**Figure 1b**). This allows us to dynamically tune transcription and translation rates of a gene to modify the overall rate of protein production. Each sensor consists of a transcription factor (TetR and LacI sensitive to aTc and IPTG, respectively) that represses its cognate promoter until an associated small molecule is present (**Figure 1b**). The small molecules bind their cognate transcription factor, altering its conformation and limiting its ability to repress the promoter, thereby turning on transcription of the downstream gene. Yellow fluorescent protein (YFP) was used as the output from the TES (**Figure 1b**) to allow us to measure the rate of protein production in single cells using flow cytometry.

Characterization of the device was performed in *Escherichia coli* cells grown in different concentrations of aTc (input) and IPTG (tuner). Steady state fluorescence measurements of single cells in exponential growth phase were taken using flow cytometry and promoter activities of both the main and tuner input were measured in relative promoter units (RPUs) to allow for direct comparisons (**Materials and Methods**; **Supplementary Figure S1**). A further advantage of characterizing our devices in RPUs is that this data can be immediately used within genetic design automation software like Cello [7], allowing our parts to be interfaced with a large library of existing sensors and logic gates[33,35].

For a fixed tuner promoter activity, we observed a sigmoidal increase in output YFP fluorescence as the input promoter activity increased from 0.002 to 6.6 RPU (**Figure 1c**). As the activity of the tuner promoter increased from 0.002 to 2.6 RPU, the entire response function shifted upwards to higher output YFP fluorescence levels. Notably, this shift was not uniform, with larger relative increases seen for lower input promoter activities; 28-fold versus 4.5-fold for inputs of 0.002 and 6.6 RPU, respectively (**Figure 1c**). Closer analysis of the flow cytometry data (**Figure 1d**), showed that these changes arose from the distributions of output YFP fluorescence for low and high inputs shifting uniformly together as the tuner promoter activity was increased. Therefore, even though a similar relative difference between outputs for low and high inputs (also referred to as the dynamic range) was observed for all tuner inputs, when the tuner input is low, the distributions are virtually identical to the autofluorescence of the cells (**Figure 1d**). This leads to even small absolute differences in the median values between low and high input states resulting in high fold-changes.

Flow cytometry data also showed a significant overlap in the output YFP fluorescence distributions for low and high input promoter activities (**Figure 1d**). Many applications require that ‘on’ and ‘off’ states in a system are well separated so that each can be accurately distinguished (e.g. for Boolean logic). To assess this separation in the TES, we calculated the fractional overlap between the output YFP fluorescence distributions for low and high input

promoter activities (**Materials and Methods**). We found a constant intersection of ~70% across all tuner promoter activity levels (**Figure 1e**), which resulted from the similar shifts we see in output across all input promoter activities (**Figure 1d**).

To better understand these effects, we derived a deterministic ordinary differential equation (ODE) model of the system (**Supplementary Text S1**). Simulations of this model for biologically realistic parameters (**Supplementary Table S1**) showed similar qualitative behavior to the experiments; increasing tuner promoter activity shifted the response curve to higher output protein production rates (**Figure 1f**). However, unlike the experiments, increases in the tuner promoter activity resulted in a small increase in the fold-change in the output between low and high inputs (**Figure 1g**, bottom). The limiting effect that the tuner sRNA can have is a possible mechanism that could account for the non-linear response observed in the experiments, whereby 'on' states do not increase as quickly as 'off' states as the tuner activity increases (**Figure 1g**, top). Because the tuner sRNA concentration is fixed for each response function, its concentration could be higher than the concentration of THS transcript when the main input is low, while also being much lower when the main input is high. This would cause the rate of protein production to be limited by the THS transcript concentration at low inputs, and by the tuner sRNA concentration at high inputs.

Another potential cause of this non-linear response could be retroactivity that occurs when the behavior of components in a biological circuit change once interconnected [36,37]. Such effects break modularity in the system and can make it difficult to predict the behavior of larger complex circuits. To explore this aspect further, we coupled our existing model to another that is able to capture retroactivity-like effects due to shifts in ribosome allocation between endogenous genes and synthetic constructs, such as the TES (**Supplementary Text S2**) [28,36,37]. Ribosomes are a key cellular resource and fluctuations in their availability due to the additional burden of a synthetic construct can cause drops in protein synthesis rates across the cell, affecting upstream components in a circuit [25,27,29,32]. Comparisons between the original models and this coupling variant, showed that retroactivity did have an effect for biologically realistic parameters, but only when the output caused a significant burden on the cell and only for the most highly expressed outputs, i.e., when both the input and tuner promoter activities were high (**Supplementary Figure S2**).

Design and assembly of a tunable genetic NOT gate

Some genetic devices rely on the expression of proteins such as transcription factors to implement basic logic functions that can be composed to carry out more complex decision-making tasks [4,7,8]. One such commonly used device is a NOT gate, which has a single input and output [33]. The function of this gate is to "invert" the input such that the output is high if the input is low and vice versa. Such a behavior can be implemented by using promoters as the

input and output, with the input promoter driving expression of a repressor protein that binds to the DNA of the constitutive output promoter. When the input promoter is inactive, the repressor is not synthesized and so the constitutive output promoter is active. However, once the input promoter is activated, the repressor is expressed which binds the output promoter and represses its activity.

Because the activity range of promoters varies, the transition point, whereby sufficient concentrations of repressor are present to cause strong repression of the output promoter, may make it impossible to connect other devices and ensure a signal is correctly propagated. For example, the output promoter of a weak sensor system acting as input to a NOT gate with a high transition point may produce insufficient repressor, causing the output promoter to be continually active. These incompatibilities can sometimes be corrected for by modifying other regulatory elements in the design. In the case of a repressor-based NOT gate, while the promoters cannot be easily changed, in bacteria the translation initiation rate can be varied by altering the ribosome binding site (RBS) for the repressor gene. Increasing the RBS strength causes more repressor protein to be produced for the same input promoter activity, shifting the transition point to a lower value [7,33]. While such modifications can fix issues with device compatibility, they require reassembly of the entire genetic device.

Given that the TES allows for the rates of both transcription and translation to be dynamically controlled, we attempted to create a proof-of-concept “tunable” NOT gate that integrated the TES to allow its response function, and crucially the transition point, to be altered after physical assembly. We chose an existing NOT gate design [33] that uses the PhlF repressor to control the activity of an output P_{phlF} promoter (**Figure 2a**). Expression of PhlF was controlled by the TES (replacing the YFP reporter protein in the original TES design; **Figure 1a**). Unlike the TES, the tunable NOT gate uses promoters for both inputs and outputs allowing it to be easily connected to other devices that use RNAP flux as an input/output signal [7,21] (**Figure 2a**).

To enable characterization of the tunable NOT gate, the output promoter P_{phlF} was used to drive expression of YFP. Measurements were taken using flow cytometry for cells harboring the device in varying concentrations of aTc and IPTG, and steady state response functions were generated (**Figures 2b** and **2c**). As expected, these displayed a negative sigmoidal shape with transition points (*K* values from the Hill function fits to the experimental data) that varied over a 7-fold range (**Figure 2b**). We also found that increases in the tuner promoter activity lead to transitions at lower activity levels for the input promoter. The range of transition points achieved by our device also covered a high proportion (35%) of the largest collection of repressor-based NOT gates built to date (total of 20 variants; **Figure 2d**) [7].

These results demonstrate the ability of the proposed TES component to dynamically alter a key characteristic of a NOT gate’s response function (specifically the transition point)

197 to improve its compatibility with other genetic devices. However, it came at a cost; tuning
198 resulted in a drop in the fold-change between low and high outputs (**Figure 2e**) and an
199 increase in the overlap of the output YFP fluorescence distributions, which made high and low
200 states difficult to distinguish (**Figure 2f**).
201
202 ***Boosting sRNA levels improves the performance of the tunable genetic devices***
203 For the THS to function correctly, it is essential that the sRNA reaches a sufficiently high
204 concentration relative to the THS transcript to ensure the associated RBS is in a predominantly
205 exposed state [34]. In our design, the tuner promoter P_{tac} has less than half the maximum
206 strength of the main input promoter P_{tet} (**Supplementary Figure S1**). Furthermore, although
207 the tuner sRNA contains a hairpin to improve its stability, sRNAs are generally more quickly
208 turned over than normal transcripts [38,39], yielding much lower steady state concentrations
209 compared to the THS transcript.
210 To better understand the role that the THS transcript to tuner sRNA ratio had on the
211 performance of the TES, we used our mathematical model of the system (**Supplementary**
212 **Text S1**) to explore how various key parameters (e.g. transcription rates and binding affinities)
213 affected the response function of the device. Using biologically realistic ranges of parameters
214 (**Supplementary Table S1**), we found that for lower sRNA transcription rates the output
215 response function could be shifted maintaining a similar fold-change between low and high
216 output states (**Figure 3a**). At these low THS/sRNA ratios the translation rate from the THS
217 transcript is limited by the sRNA concentration. However, as the sRNA transcription rate
218 increased a transition point was seen (i.e. between green and blue shared curves in **Figure**
219 **3a**) whereby for low THS transcription rates the sRNAs are in excess making the output protein
220 production rate limited by the THS transcript concentration (**Figure 3a**). In contrast, at high
221 THS transcription rates the sRNAs become limiting again but allow for relatively much higher
222 output protein production rates that enable a larger fold-change in the response function of
223 the TES (**Figure 3a**). Further stochastic modelling of the system showed that increased sRNA
224 transcription rates also reduced variability in the distribution of protein production rates across
225 a population and lowered the fractional intersection between low and high output states
226 (**Figure 3b**).
227 To experimentally verify the benefit of increasing the sRNA transcription rate, we built
228 a complementary sRNA booster plasmid that contained a high-copy pColE1 origin of
229 replication (50–70 copies per cell) [40] and expressed the tuner sRNA from a strong viral P_{T7}
230 promoter (**Figure 3c**) [41]. Transcription from P_{T7} requires T7 RNA polymerase (T7RNAP). This
231 is provided by our host strain *E. coli* BL21 Star (DE3), which has the *T7RNAP* gene under the
232 control of an IPTG inducible P_{lacUV5} promoter within its genome (**Figure 3c**) [42]. Using IPTG,
233 induction of the tuner P_{tac} promoter in our devices using IPTG leads to simultaneous

234 expression of T7 RNAP from the host genome and transcription of additional tuner sRNA from
235 the booster plasmid (**Figure 3c**). As the tunable devices are encoded on a plasmid with a
236 p15A origin of replication (~15 copies per cell; **Supplementary Figure S3**) [43], we would expect
237 at least five times higher tuner sRNA concentrations are reached when the sRNA booster is
238 present.

239 Cells were co-transformed with each tunable genetic device and sRNA booster
240 plasmid, and their response functions were measured (**Figures 3D** and **3E**). As predicted by
241 the modelling, the TES displayed improved performance with a more than doubling in the fold-
242 change across all tuner promoter activities and a >40% drop in the intersection between low
243 and high output YFP fluorescence distributions (**Table 1**). For the tunable NOT gate only minor
244 differences in performance were seen with mostly small decreases in fold-change for high
245 tuner promoter activities.

246

247 ***Self-cleaving ribozyme insulators impact toehold switch function***

248 In our initial designs, a RiboJ self-cleaving ribozyme was included in the TES and NOT gate
249 to insulate the translation of the *yfp* or *phlF* genes, respectively, from different 5' untranslated
250 region (UTR) sequences that might be generated when using different promoters as an input
251 (**Figures 1a, 2a**) [44]. Any variable UTR sequences would be cleaved at the RiboJ site to
252 produce a standardized mRNA with more consistent rates of mRNA degradation and
253 translation. Unfortunately, because RiboJ contains a number of strong secondary RNA
254 structures [44,45], it is possible that the 23 nt hairpin at the 3'-end impacts the ability for the sRNA
255 to interact with the THS, reducing the hybridization rate (**Figure 4a**).

256 To assess whether the RiboJ insulator might affect the stability of secondary structures
257 that are crucial to the TES's function, we performed thermodynamic modelling of the binding
258 between the toehold switch region of the mRNA and the tuner sRNA for variants of the TES
259 design with and without RiboJ present (**Materials and Methods**). Simulations showed a 40%
260 drop in predicted Gibbs free energy of the reactants when RiboJ was removed (−40.5 kcal/mol
261 with versus −65 kcal/mol without RiboJ; **Figure 4b**). This suggests that binding between
262 sRNAs and the THS may be hampered by interactions with the RiboJ insulator, lowering the
263 effective translation initiation rate of the RBS controlled by the toehold switch and
264 subsequently the overall performance of the devices.

265 To experimentally test these predictions, non-insulated variants of the TES and tunable
266 NOT gate were constructed in which RiboJ was removed. Characterization of these devices
267 showed major improvements in overall performance (**Figures 4c** and **4d**). The TES saw more
268 than a doubling in the dynamic range and 10-fold increase in the fold-change between 'on'
269 and 'off' states across low and high tuner activity levels compared to the original design (**Table**
270 **1**). In addition, the fraction of intersection of the output YFP fluorescence distributions dropped

271 by >50%. The tunable NOT gate saw more modest improvements with a 73% increase in the
272 fold-change at high tuner activity levels, but an overall drop of 66% in the range of transition
273 points (*K* values) that could be achieved (**Table 1**). These results highlight an important
274 consideration often ignored. When using RNA-based devices that require proper formation of
275 secondary structures, care must be taken in looking at how multiple devices relying on mRNA
276 folding to function could interfere with each other, leading to cryptic failure modes.

277 Another counterintuitive change in the TES's response function after RiboJ removal
278 was the large drop in output YFP fluorescence from 26 to 3 arbitrary units (a.u.) when no input
279 or tuner was present (**Figure 4c**). Similar drops of between 4- and 11-fold were also seen for
280 higher tuner promoter activities. Given that binding of a tuner sRNA to the THS mRNA should
281 be less hampered when RiboJ is absent, an increase not decrease in output protein production
282 would be expected. A possible explanation is that the stability of the THS mRNA decreased
283 after RiboJ was removed. This is supported by recent results that have shown the RiboJ
284 insulator both stabilizes its mRNA and also boosts the translation initiation rate of a nearby
285 downstream RBS [46]. The precise mechanisms for this are not well understood but it is thought
286 that the structural aspect of the RiboJ element at the 5'-end of an mRNA inhibits degradation
287 by exonucleases, whilst the hairpin at the 3'-end of RiboJ exposes the nearby RBS by reducing
288 the chance of unwanted secondary structure formation [44,45].

289 Finally, we combined the non-insulated designs with the sRNA booster plasmid to see
290 whether further improvements could be made (**Table 1**). For the TES, we found that the
291 dynamic range had plateaued, with only moderate increases that were mostly at low tuner
292 promoter activities. In contrast, the fold-change between low and high outputs more than
293 doubled across tuner promoter activities when compared to the non-insulated design, and a
294 further drop of >18% was seen in the fractional intersection between the YFP fluorescence
295 distributions for these output states. The tunable NOT gate showed minor decreases in
296 performance for many of the measures (**Table 1**). However, the inclusion of the sRNA booster
297 likely increased overall PhlF concentrations as the transition points from an 'on' to 'off' state
298 (*K* value range) shifted to far below what had been seen for all other designs. This would make
299 this specific design of value for uses where a weak input signal needs to be inverted and
300 amplified simultaneously.

301

302 ***Towards complex tunable logic***

303 To create larger genetic circuits that implement complex logic, it is vital that a sufficiently
304 diverse set of logic gates are available for use. Because a NOT gate alone has limited
305 capabilities, we further modified its design to create a tunable 2-input NOR gate device [7,33].
306 The output of a NOR gate is 'on' only when both inputs are 'off' (**Figure 5b**) and crucially this
307 type of logic gate is functionally complete (i.e. any combinatorial logic function can be

308 implemented using NOR gates alone). In our new device, we added a further inducible input
309 promoter, P_{BAD}, directly before the existing P_{tet} input promoter, and included the associated
310 sensor system (i.e. *araC* gene) to allow activity of the P_{BAD} promoter to be controlled by the
311 concentration of L-Arabinose (**Figure 5a**). Our modifications were made to the existing NOT
312 gate design that included the RiboJ insulator because this produced the largest tunable range
313 for the 'on' to 'off' transition point.

314 To assess the function of the tunable NOR gate, the activities of both input promoters
315 P_{BAD} and P_{tet}, and the tuner promoter P_{tac} were varied by culturing cells harboring the device
316 in different concentrations of L-Arabinose, aTc and IPTG, respectively (**Materials and**
317 **Methods**). The two-dimensional response functions from these experiments (**Figure 5c**)
318 showed that NOR logic was successfully implemented and that the transition point from low
319 to high output for both inputs was simultaneous shifted to lower input promoter activities when
320 the tuner promoter was highly active (**Figure 5c**, right panel). Considering each input promoter
321 separately, this resulted in the transition point between 'on' and 'off' states shifting by 16- and
322 6-fold for P_{BAD} and P_{tet}, respectively.

323 Interestingly, unlike the NOT gate, even at high tuner promoter activities, the dynamic
324 range was better maintained, dropping at most 35%, and the fold-change between 'on' and
325 'off' states remained above 4- and 8-fold for low and high tuner promoter activities, respectively
326 (**Supplementary Table S3**). Furthermore, the improved separation of these states leads to
327 smaller intersections in the output YFP distributions compared to the NOT gate. This was
328 especially evident when comparing NOR gate states where both input promoters were
329 simultaneously 'off' or 'on' with only a ~5% intersection (**Supplementary Table S3**).

330 The cause of this improvement is not clear but may relate to the P_{BAD} promoter
331 insulating expression of the *phlF* gene from transcriptional read-through originating from the
332 tuner transcription unit that is located directly upstream in the DNA (**Supplementary Figure**
333 **S3**). Without this insulating effect, read-through would cause elevated expression of PhlF,
334 even when the input promoters are off, and potentially lead to a partial switch in the output
335 when the tuner promoter is active (as seen for the original NOT gate, **Figure 2b**). Such a
336 mechanism could also account for the elevated output levels for the TES when the input
337 promoter is off, but the tuner promoter activity is increased (**Figure 1c**).

338

339 ## Discussion

340 In this work, we have developed a new class of genetic device where an additional tuner input
341 is able to dynamically change key features of the device's response function. This was
342 achieved by employing a regulatory motif that allows for the transcription and translation rate
343 of a gene to be controlled by the activity of multiple input promoters. Connecting this TES to

344 a number of small molecule sensors, we were able to demonstrate its ability to shift the 'on'
345 and 'off' output states by 4.5- and 28-fold, respectively (**Figure 1**). Furthermore, we showed
346 how the TES could be incorporated into genetic NOT and NOR gates to enable tuning of the
347 crucial transition point between an 'on' and 'off' state over >6-fold range (**Figure 2**). This made
348 the gates more broadly compatible with other components where matching of transition points
349 to high and low output levels is essential for effective propagation of biological computations
350 [7,22]. Unfortunately, the performance of the tunable devices varied for differing tuner inputs,
351 leading to a trade-off between performance and the level of tuning required. Mathematical and
352 biophysical modelling of the TES helped to uncover: 1. the importance of ensuring sufficient
353 tuner sRNA is present to fully activate the THS (**Figure 3**), and 2. the presence of possible
354 detrimental interactions between a self-cleaving ribosome used to insulate protein expression
355 from genetic context and the THS that relies on the correct folding of an RNA secondary
356 structure to function properly (**Figure 4**). Modified designs that addressed these concerns
357 demonstrated improved performance for the TES in both cases, but only minor improvements
358 in the fold-change of the tunable NOT gate when the self-cleaving ribosome was removed
359 (**Table 1**). By combining these two modifications into a single system, further improvements
360 were observed for the TES, but not the tunable NOT gate when compared to the original
361 designs (**Table 1**). In contrast, the NOR gate behaved more consistently across tuner activity
362 levels and displayed better performance with greater separation of 'on' and 'off' states. To the
363 best of our knowledge the simultaneous control of transcription and translation to tune the
364 response function of a genetic device has not been shown before, making this work a valuable
365 resource for others to build on. Furthermore, unlike other attempts at tuning the response of
366 devices through mutation of protein components to alter catalytic rates [47], our method allows
367 for dynamic changes to a response function using simple to control transcriptional signals (i.e.
368 by the use of appropriate promoters).

369 A difficulty when using THSs to regulate gene expression is that high relative
370 concentrations of sRNA are required to achieve a strong enough activation of mRNA
371 translation. This stems from the regulatory mechanism relying purely on base-pairing of the
372 sRNA to THS, which places limits on the binding affinity that can be achieved. A possible
373 means of increasing the affinity between these species would be to exploit RNA chaperones
374 such as Hfq [48,49]. In prokaryotes, sRNAs that associate with Hfq play a variety of roles from
375 inhibiting and activating translation, to affecting the stability of a target mRNA [50–52]. In some
376 cases, these effects are significant. For example, it has been shown *in vitro* that Hfq increases
377 by 30- to 50-fold the binding affinity of the DsrA sRNA to the leader of the *rpoS* mRNA [53].
378 Designing *de novo* sRNA that binds to Hfq to increase their affinity to a target mRNA has been
379 demonstrated for both activation [48] and inhibition [49] of translation initiation. In both cases, Hfq
380 binding scaffolds from endogenous genes (e.g. *micC*) are fused with a targeting sequence.

This approach could be employed in future TES designs. In fact, previous work that used Hfq associated sRNAs to implement a metabolically cheap negative feedback control loop created a useful repressive tuning element that could be directly used in our system[49]. By combining the findings from that study with ours and incorporating recent improvements in THS design [6], it should be possible to make further strides towards high-performance tunable genetic devices.

An interesting future direction opened up by the adaptive nature of our devices is the possibility of incorporating many of them into larger circuits. This would allow many parts of a circuit to be tuned simultaneously to maximize the compatibility between components and optimize the behavior of the overall system. Unlike a typical design-build-test cycle that requires the reassembly of a genetic circuit with a new combination of parts if malfunctions are detected, this work supports a design-build-test-*tune* cycle where time consuming and costly reassembly can be avoided. Rather than reassembling a circuit after each cycle, parts can instead be dynamically tuned until they work correctly in unison. In this context, the use of sensitivity analysis during circuit design would offer valuable insight into specific components where even small deviations in behavior would adversely impact overall circuit function [54]. These would be ideal candidates to be encoded using tunable devices to allow for tweaking at these critical points. Furthermore, the use of new microfluidic culturing systems and online machine learning algorithms offers a way to rapidly discover the precise tuner inputs needed to achieve specific circuit functions under fluctuating environmental conditions [55–58].

Some practical challenges are raised by the additional tuner input in our devices. Systems composed of numerous tunable devices will require a large number of tuner inputs to be controlled simultaneously. If external signals are to be used, then a unique sensor is required for each tuner input, as well as the capability to be able to control the environment to provide the correct set of input signals over time. Although the range of small molecule [35] and light based [47,59] sensing systems available to bioengineers in *E. coli* has grown over recent years, the ability to control many environmental factors (e.g. small molecule concentrations and light intensities) simultaneously remains difficult. However, external control is not the only way to tune the behavior of these devices. The use of promoters as inputs and outputs allows them to be controlled by connecting them directly to the many transcriptional signals used natively in a cell. This offers the advantage of tapping into the cells innate capacity to sense and respond to its environment and internal protein synthesis demands. Alternatively, if an adaptive circuit is not required, sensors controlling the tuning inputs could be replaced once a working configuration is found with constitutive promoters of an identical strength. This would still reduce the reassembly required to a single step once the correct combination of tuning

inputs is found and remove the need for active control of the environment to provide necessary stimuli for sensors.

When designing our tunable devices, we observed deviations between the experimental and modelled responses. Further investigation suggested that this may be due to retroactivity [36,37], specifically whereby expression of the output reporter protein places a significant burden on the host cell (**Supplementary Text S2**). Recently, there has been increased interest in the role of burden [60] impacting upon the function of large synthetic genetic systems and attempts made to help mitigate its effect [61]. One approach has been to create intracellular resource allocation schemes based on split exogenous RNAPs [62]. These limit the maximum burden a circuit can impose by providing pools of transcriptional resources that are orthogonal to the endogenous ones. This helps to reduce the chance of large unpredictable physiological changes in the cell that might affect the function of synthetic circuits. Because our tunable devices can have their sensitivity dynamically altered (i.e. transition point can occur for weaker inputs), they offer another means of adapting to the reduced availability of shared cellular resources. They could also be used to boost the expression of downstream components to mitigate retroactivity effects or even be used to cap to maximum levels of resource that can be used by a circuit (i.e. tuning the levels of several devices concurrently to ensure protein expression does not exceed a fixed level).

For synthetic biology to have a broad and lasting impact outside of the carefully controlled conditions of a lab, it is vital that means are developed to construct adaptive genetic circuits able to maintain their functionality when exposed to unexpected environmental changes or shifts in host cell physiology [63]. By combining advances in biological control engineering [61,63–67] with the tunable genetic devices developed in this work, bioengineers have a complementary set of tools capable of taking steps towards this goal.

Materials and Methods

Strains and media

Cloning was performed using *Escherichia coli* strain DH5-α (F^- *endA*1 *glnV*44 thi-1 *recA*1 *relA*1 *gyrA*96 *deoR nupG purB*20 φ80d*lacZ*ΔM15 Δ(*lacZYA–argF*)U169, *hsdR*17($r_K^-m_K^+$), λ^-) (New England Biolabs, C2987I). Device characterization was performed using BL21 Star (DE3) (F^- *ompT hsdS*$_B$ (r_B^-, m_B^-) *gal dcm rne*-131 [DE3]) (Thermo Fisher Scientific, C601003). For cloning, cells were grown in LB Miller broth (Sigma-Aldrich, L3522). For device characterization, cells were grown in M9 minimal media supplemented with glucose containing M9 salts (6.78 g/L Na_2HPO_4, 3 g/L KH_2PO_4, 1 g/L NH_4Cl, 0.5 g/L NaCl) (Sigma-Aldrich, M6030), 0.34 g/L thiamine hydrochloride (Sigma T4625), 0.4% D-glucose (Sigma-Aldrich, G7528), 0.2% casamino acids (Acros, AC61204-5000), 2 mM $MgSO_4$ (Acros, 213115000),

453 and 0.1 mM $CaCl_2$ (Sigma-Aldrich, C8106). Antibiotic selection was performed using 50 µg/mL
454 kanamycin (Sigma-Aldrich, K1637) or 50 mg/mL spectinomycin (Santa Cruz Biotechnology,
455 sc-203279). Induction of sensor systems was performed using anhydrotetracycline (aTc)
456 (Sigma-Alrdich, 37919), isopropyl β-D-1-thiogalactopyranoside (IPTG) (Sigma-Aldrich, I6758)
457 and L-Arabinose (Ara) (Sigma-Aldrich, A3256).
458
459 ***Genetic device synthesis and assembly***
460 Plasmids containing the TES and tunable NOT gate devices were constructed by gene
461 synthesis of the individual transcriptional units (e.g. tuner sRNA, THS-*yfp*, THS-*phlF* and *yfp*),
462 (GeneArt, Thermo Fisher Scientific) and insertion of these elements into a pAN1201 plasmid
463 backbone. pAN1201 provides all the sensor systems used for induction of the input promoters.
464 Assembly was performed by first PCR of the synthesized transcriptional units and the
465 pAN1201 plasmid (without the *lacZα* region normally used for blue/white screening) with all
466 primers containing a 20 bp tail homologous sequence to the previous or subsequent region in
467 the desired assembly. Gibson assembly (New England Biolabs, E2611S) was then used to
468 scarlessly assemble these fragments into a complete plasmid. The plasmid used to boost
469 tuner sRNA levels (pVB005) was fully synthesized (GeneArt, Thermo Fisher Scientific). The
470 plasmid containing the tunable NOR gate device (pVB006) was constructed by first PCR
471 amplification of the pAN1720 plasmid (without the *lacZα* region normally used for blue/white
472 screening) using primers containing an EcoRI restriction site at the 5'-end and a NotI restriction
473 site at the 3'-end. The tunable NOR gate DNA insert was synthesized in three parts (Integrated
474 DNA Technologies) which were assembled using a standard Golden Gate assembly method
475 (New England Biolabs, E1601S) to create a full-length linear insert. This was designed to
476 contain complementary EcoRI and NotI restriction sites to the amplified pAN1720 fragment.
477 Both linear DNA fragments were finally used in a standard restriction digest using EcoRI (New
478 England Biolabs, R3101) and NotI (New England Biolabs, R3189), and then a ligation reaction
479 (New England Biolabs, M0202S) to assemble the complete pVB006 plasmid. All plasmids
480 were sequence verified by Sanger sequencing (Eurofins Genomics). Annotated plasmid maps
481 of all devices are provided in **Supplementary Figure S3** and **Supplementary File S2**.
482
483 ***Genetic device characterization***
484 Single colonies of cells transformed with the appropriate genetic constructs were inoculated
485 in 200 µL M9 media supplemented with glucose and necessary antibiotics for selection in a
486 96-well microtiter plate (Thermo Fisher Scientific, 249952) and grown for 16 hours in a shaking
487 incubator (Stuart, S1505) at 37 °C and 1250 rpm. Following this, cultures were diluted 9:1600
488 (15 µL into 185 µL, with 15 µL of this dilution loaded into 185 µL) in glucose supplemented M9
489 media with necessary antibiotics for selection and grown for 3 hours at the same conditions.

490 Next, the cultures were diluted 1:45 (10 µL into 140 µL) into supplemented M9 media with
491 necessary antibiotics for selection and any required inducers in a new 96-well microtiter plate
492 (Thermo Fisher Scientific, 249952) and grown at 37 °C and 1250 rpm for 5 hours. Finally, the
493 cells were diluted 1:10 (10 µL into 90 µL) in phosphate-buffered saline (PBS) (Gibco,18912-
494 014) containing 2 mg/mL kanamycin to halt translation and incubated at room temperature for
495 1 hour to allow for maturation of the YFP before performing flow cytometry.
496
497 ***Flow cytometry***
498 YFP fluorescence of individual cells was measured using an Acea Biosciences NovoCyte
499 3000 flow cytometer equipped with a NovoSampler to allow for automated collection from 96-
500 well microtiter plates. Cells were excited using a 488 nm laser and measurements were taken
501 using a 530 nm detector. A flow rate of 40 µL/min was used to collect at least 10^5 cells for all
502 measured conditions. Automated gating of events using the forward (FSC-A) and side scatter
503 (SSC-A) channels was performed for all data using the FlowCal Python package version 1.2
504 [68] and the density2d function with parameters: channels = ['FSC-A', 'SSC-A'], bins = 1024,
505 gate_fraction = 0.5, xscale = 'logicle', yscale = 'logicle', and sigma = 10.0.
506
507 ***Autofluorescence correction***
508 To measure YFP fluorescence from our constructs it was necessary to correct for the
509 autofluorescence of cells. An autofluorescence control strain containing the pAN1201 plasmid
510 [7], which does not express YFP but contains the same backbone as our genetic devices, was
511 measured using flow cytometry under the same culturing conditions as for characterization.
512 Measurements were taken from three biological replicates and an average of the medians of
513 the gated distributions was subtracted from the gated YFP fluorescence flow cytometry data
514 of the characterized devices, as in previous work [7].
515
516 ***Characterization of sensor systems in relative promoter units (RPU)***
517 To allow for inputs to our devices to be controlled in standardized relative promoter units
518 (RPUs) [7,69], calibration curves for the two sensor systems were generated to enable a
519 conversion between a chemical inducer concentration and the relative promoter activity of
520 each sensors' output promoter (P_{tac} and P_{tet}). Cells transformed with plasmids pAN1718 and
521 pAN1719 for P_{tac} and P_{tet}, respectively, and the pAN1717 RPU standard [7], were cultured in
522 the same way as the characterization experiments. Flow cytometry was used to measure YFP
523 fluorescence which was further corrected for cell autofluorescence. RPU values were then
524 calculated by dividing the YFP output from the sensor by the YFP output from the RPU
525 standard and a Hill function fitted to the resultant data (**Supplementary Figure S1**).
526

527 ***Quantifying histogram intersections***

528 The fraction of intersection *H* between two histograms (e.g. flow cytometry fluorescence
529 distributions), *x* and *y*, was calculated using,

530 $$H(x,y) = \sum_{i=1}^{n} \frac{\min(x_i, y_i)}{x_i}. \quad (1)$$

531 Here, histograms *x* and *y* are divided into *n* bins that correspond to identical ranges of values
532 for each, with x_i and y_i denoting the value of bin *i* for histogram *x* or *y*, respectively.

533

534 ***Predicting RNA binding and secondary structure***

535 To predict the binding and secondary structure of the toehold switch and tuner sRNA (**Figure**
536 **3**), thermodynamic modelling was performed using the NUPACK web application [70]. All
537 simulations were run using the parameters: nucleic acid = RNA, temperature = 37 °C and the
538 concentration of toehold switch mRNA was set to 5×10^{-4} μM. The switch sequence mRNA
539 and the switch sequence mRNA with an upstream cleaved RiboJ were simulated
540 independently with additional parameters strand species = 1 and a maximum complex size =
541 1. The toehold switch mRNA with and without an upstream RiboJ sequence where also
542 simulated in the presence of trigger sRNA set to a concentration of 7×10^{-5} μM with additional
543 parameters: strand species = 1 and a maximum complex size = 1. Full sequences are given
544 in **Supplementary Table S2**.

545

546 ***Computational analyses and data fitting***

547 All computational analyses were performed using Python version 3.6.6. Response functions
548 for the TES designs were generated by fitting median values of YFP fluorescence from flow
549 cytometry data to a Hill function of the form

550 $$y = y_{\min} + (y_{\max} - y_{\min}) \frac{x^n}{K^n + x^n}, \quad (2)$$

551 where *y* is the output YFP fluorescence (in arbitrary units), $y_{\min}$ and $y_{\max}$ are the minimum and
552 maximum output YFP fluorescence (in arbitrary units), respectively, *K* is the input promoter
553 activity (in RPU units) at which the output is halfway between its minimum and maximum, *n* is
554 the Hill coefficient, and *x* is the input promoter activity (in RPU units). Response functions for
555 the tunable NOT gates were generated in a similar way using a Hill function of the form

556 $$y = y_{\min} + (y_{\max} - y_{\min}) \frac{K^n}{K^n + x^n}. \quad (3)$$

557 Fitting of data was performed using non-linear least squares and the curve_fit function from
558 the SciPy.integrate Python package version 1.1.

559

560 ***Numerical simulation***

The deterministic ODE model (**Supplementary Text S1**) was simulated using the odeint function of the SciPy.integrate Python package version 1.1 with default parameters. The delay differential equations (**Supplementary Text S2**) were simulated using the DifferentialEquations module version 6.10 using the Bogacki-Shampine 3/2 method running in Julia version 1.3. Stochastic simulations of the biochemical model (**Supplementary Text S1**) were performed using the tau-leap method in COPASI [71] version 4.24 with the following settings: number of iterations (simulations) = 4000, duration = 100 min, interval size = 1 min, number of intervals = 100 and the starting in steady state option selected. Initial steady-state conditions for the simulation are calculated automatically by COPASI using a damped Newton method.

Visualization of genetic designs

All genetic diagrams are shown using Synthetic Biology Open Language Visual (SBOL Visual) notation [72]. SBOL Visual diagrams were generated using the DNAplotlib Python package [73,74] version 1.0 which were then annotated and composed with OmniGraffle version 7.9.2.

Data availability

Systems Biology Markup Language (SBML) file implementing a model of the TES can be found in **Supplementary File S1**. Annotated sequence files in GenBank format for all plasmids are available in **Supplementary File S2**. All plasmids are available from Addgene (#127185–127189).

Acknowledgements

The authors wish to acknowledge the assistance of Dr. Andrew Herman and Dr. Lorena Sueiro Ballesteros of the University of Bristol Faculty of Biomedical Sciences Flow Cytometry Facility, and Bettina Frank of the Anderson Lab for help in preliminary plate reader assays. This work was supported by BrisSynBio, a BBSRC/EPSRC Synthetic Biology Research Centre grant BB/L01386X/1 (M.d.B., T.E.G.), EPSRC/BBSRC Centre for Doctoral Training in Synthetic Biology grant EP/L016494/1 (V.B.), the EU Horizon 2020 research project COSY-BIO grant 766840 (M.d.B), and a Royal Society University Research Fellowship grant UF160357 (T.E.G.)

Author Contributions

T.E.G. conceived of the study. V.B., T.E.G. and G.A.M. performed the experiments. V.B., M.d.B. and T.E.G. developed the mathematical models. V.B. analyzed the data. T.E.G., V.B., M.d.B. and G.A.M. wrote the manuscript.

Conflicts of Interest

The authors declare no competing financial interests.

600 ## References

601 1. Brophy, J. A. N. & Voigt, C. A. Principles of genetic circuit design. *Nat. Methods* **11**, 508
602 (2014).
603 2. Greco, F. V., Tarnowski, M. J. & Gorochowski, T. E. Living computers powered by
604 biochemistry. *The Biochemist* **41**, 14–18 (2019).
605 3. Slomovic, S., Pardee, K. & Collins, J. J. Synthetic biology devices for in vitro and in vivo
606 diagnostics. *Proc. Natl. Acad. Sci.* **112**, 14429 (2015).
607 4. Andrews, L. B., Nielsen, A. A. K. & Voigt, C. A. Cellular checkpoint control using
608 programmable sequential logic. *Science* **361**, eaap8987 (2018).
609 5. Bashor, C. J. *et al.* Complex signal processing in synthetic gene circuits using
610 cooperative regulatory assemblies. *Science* **364**, 593 (2019).
611 6. Green, A. A. *et al.* Complex cellular logic computation using ribocomputing devices.
612 *Nature* **548**, 117 (2017).
613 7. Nielsen, A. A. K. *et al.* Genetic circuit design automation. *Science* **352**, aac7341 (2016).
614 8. Moon, T. S., Lou, C., Tamsir, A., Stanton, B. C. & Voigt, C. A. Genetic programs
615 constructed from layered logic gates in single cells. *Nature* **491**, 249 (2012).
616 9. Gao, X. J., Chong, L. S., Kim, M. S. & Elowitz, M. B. Programmable protein circuits in
617 living cells. *Science* **361**, 1252 (2018).
618 10. Daniel, R., Rubens, J. R., Sarpeshkar, R. & Lu, T. K. Synthetic analog computation in
619 living cells. *Nature* **497**, 619 (2013).
620 11. Fernandez-Rodriguez, J., Yang, L., Gorochowski, T. E., Gordon, D. B. & Voigt, C. A.
621 Memory and Combinatorial Logic Based on DNA Inversions: Dynamics and
622 Evolutionary Stability. *ACS Synth. Biol.* **4**, 1361–1372 (2015).
623 12. Hsiao, V., Hori, Y., Rothemund, P. W. & Murray, R. M. A population-based temporal
624 logic gate for timing and recording chemical events. *Mol. Syst. Biol.* **12**, 869 (2016).
625 13. Elowitz, M. B. & Leibler, S. A synthetic oscillatory network of transcriptional regulators.
626 *Nature* **403**, 335–338 (2000).
627 14. Stricker, J. *et al.* A fast, robust and tunable synthetic gene oscillator. *Nature* **456**, 516
628 (2008).
629 15. Niederholtmeyer, H. *et al.* Rapid cell-free forward engineering of novel genetic ring
630 oscillators. *eLife* **4**, e09771 (2015).
631 16. Kong, W., Meldgin, D. R., Collins, J. J. & Lu, T. Designing microbial consortia with
632 defined social interactions. *Nat. Chem. Biol.* **14**, 821–829 (2018).
633 17. Karig, D. *et al.* Stochastic Turing patterns in a synthetic bacterial population. *Proc. Natl.*
634 *Acad. Sci.* **115**, 6572–6577 (2018).

18. Cao, Y. *et al.* Programmable assembly of pressure sensors using pattern-forming bacteria. *Nat. Biotechnol.* **35**, 1087–1093 (2017).
19. Danino, T., Mondragón-Palomino, O., Tsimring, L. & Hasty, J. A synchronized quorum of genetic clocks. *Nature* **463**, 326–330 (2010).
20. Din, M. O. *et al.* Synchronized cycles of bacterial lysis for in vivo delivery. *Nature* **536**, 81–85 (2016).
21. Canton, B., Labno, A. & Endy, D. Refinement and standardization of synthetic biological parts and devices. *Nat. Biotechnol.* **26**, 787 (2008).
22. P. Vaidyanathan *et al.* A Framework for Genetic Logic Synthesis. *Proc. IEEE* **103**, 2196–2207 (2015).
23. Weinberg, B. H. *et al.* Large-scale design of robust genetic circuits with multiple inputs and outputs for mammalian cells. *Nat. Biotechnol.* **35**, 453 (2017).
24. Moser, F. *et al.* Genetic Circuit Performance under Conditions Relevant for Industrial Bioreactors. *ACS Synth. Biol.* **1**, 555–564 (2012).
25. Gorochowski, T. E., van den Berg, E., Kerkman, R., Roubos, J. A. & Bovenberg, R. A. L. Using Synthetic Biological Parts and Microbioreactors to Explore the Protein Expression Characteristics of Escherichia coli. *ACS Synth. Biol.* **3**, 129–139 (2014).
26. Cardinale, S. & Arkin, A. P. Contextualizing context for synthetic biology – identifying causes of failure of synthetic biological systems. *Biotechnol. J.* **7**, 856–866 (2012).
27. Gyorgy, A. *et al.* Isocost Lines Describe the Cellular Economy of Genetic Circuits. *Biophys. J.* **109**, 639–646 (2015).
28. Gorochowski, T. E., Avcilar-Kucukgoze, I., Bovenberg, R. A. L., Roubos, J. A. & Ignatova, Z. A Minimal Model of Ribosome Allocation Dynamics Captures Trade-offs in Expression between Endogenous and Synthetic Genes. *ACS Synth. Biol.* **5**, 710–720 (2016).
29. Qian, Y., Huang, H.-H., Jiménez, J. I. & Del Vecchio, D. Resource Competition Shapes the Response of Genetic Circuits. *ACS Synth. Biol.* **6**, 1263–1272 (2017).
30. Yeung, E. *et al.* Biophysical Constraints Arising from Compositional Context in Synthetic Gene Networks. *Cell Syst.* **5**, 11-24.e12 (2017).
31. Gorochowski, T. E. *et al.* Genetic circuit characterization and debugging using RNA-seq. *Mol. Syst. Biol.* **13**, 952 (2017).
32. Gorochowski, T. E. *et al.* Absolute quantification of translational regulation and burden using combined sequencing approaches. *Mol. Syst. Biol.* **15**, e8719 (2019).
33. Stanton, B. C. *et al.* Genomic mining of prokaryotic repressors for orthogonal logic gates. *Nat. Chem. Biol.* **10**, 99–105 (2014).
34. Green, A. A., Silver, P. A., Collins, J. J. & Yin, P. Toehold Switches: De-Novo-Designed Regulators of Gene Expression. *Cell* **159**, 925–939 (2014).

672 35. Meyer, A. J., Segall-Shapiro, T. H., Glassey, E., Zhang, J. & Voigt, C. A. Escherichia
673 coli “Marionette” strains with 12 highly optimized small-molecule sensors. *Nat. Chem.*
674 *Biol.* **15**, 196–204 (2019).
675 36. Del Vecchio, D., Ninfa, A. J. & Sontag, E. D. Modular cell biology: retroactivity and
676 insulation. *Mol. Syst. Biol.* **4**, 161 (2008).
677 37. D. Del Vecchio & E. D. Sontag. Engineering principles in bio-molecular systems: From
678 retroactivity to modularity. in *2009 European Control Conference (ECC)* 658–664
679 (2009). doi:10.23919/ECC.2009.7074478.
680 38. Chen, H., Shiroguchi, K., Ge, H. & Xie, X. S. Genome-wide study of mRNA degradation
681 and transcript elongation in Escherichia coli. *Mol. Syst. Biol.* **11**, 781 (2015).
682 39. Busi, F., Arluison, V. & Régnier, P. Absolute Regulatory Small Noncoding RNA
683 Concentration and Decay Rates Measurements in Escherichia coli. in *Bacterial*
684 *Regulatory RNA: Methods and Protocols* (eds. Arluison, V. & Valverde, C.) 231–248
685 (Springer New York, 2018). doi:10.1007/978-1-4939-7634-8_14.
686 40. Lutz, R. & Bujard, H. Independent and Tight Regulation of Transcriptional Units in
687 Escherichia Coli Via the LacR/O, the TetR/O and AraC/I1-I2 Regulatory Elements.
688 *Nucleic Acids Res.* **25**, 1203–1210 (1997).
689 41. Dunn, J. J., Studier, F. W. & Gottesman, M. Complete nucleotide sequence of
690 bacteriophage T7 DNA and the locations of T7 genetic elements. *J. Mol. Biol.* **166**, 477–
691 535 (1983).
692 42. Studier, F. W. & Moffatt, B. A. Use of bacteriophage T7 RNA polymerase to direct
693 selective high-level expression of cloned genes. *J. Mol. Biol.* **189**, 113–130 (1986).
694 43. Hiszczyńska-Sawicka, E. & Kur, J. Effect of Escherichia coli IHF Mutations on Plasmid
695 p15A Copy Number. *Plasmid* **38**, 174–179 (1997).
696 44. Lou, C., Stanton, B., Chen, Y.-J., Munsky, B. & Voigt, C. A. Ribozyme-based insulator
697 parts buffer synthetic circuits from genetic context. *Nat. Biotechnol.* **30**, 1137 (2012).
698 45. Carrier, T. A. & Keasling, J. D. Engineering mRNA stability in E. coli by the addition of
699 synthetic hairpins using a 5′ cassette system. *Biotechnol. Bioeng.* **55**, 577–580 (1997).
700 46. Clifton, K. P. *et al.* The genetic insulator RiboJ increases expression of insulated genes.
701 *J. Biol. Eng.* **12**, 23 (2018).
702 47. Landry, B. P., Palanki, R., Dyulgyarov, N., Hartsough, L. A. & Tabor, J. J. Phosphatase
703 activity tunes two-component system sensor detection threshold. *Nat. Commun.* **9**, 1433
704 (2018).
705 48. Soper, T., Mandin, P., Majdalani, N., Gottesman, S. & Woodson, S. A. Positive
706 regulation by small RNAs and the role of Hfq. *Proc. Natl. Acad. Sci.* **107**, 9602 (2010).
707 49. Kelly, C. L. *et al.* Synthetic negative feedback circuits using engineered small RNAs.
708 *Nucleic Acids Res.* **46**, 9875–9889 (2018).

50. Waters, L. S. & Storz, G. Regulatory RNAs in Bacteria. *Cell* **136**, 615–628 (2009).
51. Storz, G., Opdyke, J. A. & Zhang, A. Controlling mRNA stability and translation with small, noncoding RNAs. *Curr. Opin. Microbiol.* **7**, 140–144 (2004).
52. Gottesman, S. Micros for microbes: non-coding regulatory RNAs in bacteria. *Trends Genet.* **21**, 399–404 (2005).
53. Soper, T. J. & Woodson, S. A. The rpoS mRNA leader recruits Hfq to facilitate annealing with DsrA sRNA. *RNA* **14**, 1907–1917 (2008).
54. Feng, X. *et al.* Optimizing Genetic Circuits by Global Sensitivity Analysis. *Biophys. J.* **87**, 2195–2202 (2004).
55. Postiglione, L. *et al.* Regulation of Gene Expression and Signaling Pathway Activity in Mammalian Cells by Automated Microfluidics Feedback Control. *ACS Synth. Biol.* **7**, 2558–2565 (2018).
56. Menolascina, F. *et al.* In-Vivo Real-Time Control of Protein Expression from Endogenous and Synthetic Gene Networks. *PLOS Comput. Biol.* **10**, e1003625 (2014).
57. Bandiera, L. *et al.* On-Line Optimal Input Design Increases the Efficiency and Accuracy of the Modelling of an Inducible Synthetic Promoter. *Processes* **6**, (2018).
58. Milias-Argeitis, A., Rullan, M., Aoki, S. K., Buchmann, P. & Khammash, M. Automated optogenetic feedback control for precise and robust regulation of gene expression and cell growth. *Nat. Commun.* **7**, 12546 (2016).
59. Baumschlager, A., Aoki, S. K. & Khammash, M. Dynamic Blue Light-Inducible T7 RNA Polymerases (Opto-T7RNAPs) for Precise Spatiotemporal Gene Expression Control. *ACS Synth. Biol.* **6**, 2157–2167 (2017).
60. Ceroni, F., Algar, R., Stan, G.-B. & Ellis, T. Quantifying cellular capacity identifies gene expression designs with reduced burden. *Nat. Methods* **12**, 415–418 (2015).
61. Ceroni, F. *et al.* Burden-driven feedback control of gene expression. *Nat. Methods* **15**, 387–393 (2018).
62. Segall-Shapiro, T. H., Meyer, A. J., Ellington, A. D., Sontag, E. D. & Voigt, C. A. A ‘resource allocator’ for transcription based on a highly fragmented T7 RNA polymerase. *Mol. Syst. Biol.* **10**, 742 (2014).
63. Segall-Shapiro, T. H., Sontag, E. D. & Voigt, C. A. Engineered promoters enable constant gene expression at any copy number in bacteria. *Nat. Biotechnol.* **36**, 352 (2018).
64. Aoki, S. K. *et al.* A universal biomolecular integral feedback controller for robust perfect adaptation. *Nature* **570**, 533–537 (2019).
65. D. Fiore, A. Guarino & M. di Bernardo. Analysis and Control of Genetic Toggle Switches Subject to Periodic Multi-Input Stimulation. *IEEE Control Syst. Lett.* **3**, 278–283 (2019).

745 66. Mishra, D., Rivera, P. M., Lin, A., Del Vecchio, D. & Weiss, R. A load driver device for
746 engineering modularity in biological networks. *Nat. Biotechnol.* **32**, 1268 (2014).
747 67. Del Vecchio, D., Abdallah, H., Qian, Y. & Collins, J. J. A Blueprint for a Synthetic
748 Genetic Feedback Controller to Reprogram Cell Fate. *Cell Syst.* **4**, 109-120.e11 (2017).
749 68. Castillo-Hair, S. M. *et al.* FlowCal: A User-Friendly, Open Source Software Tool for
750 Automatically Converting Flow Cytometry Data from Arbitrary to Calibrated Units. *ACS*
751 *Synth. Biol.* **5**, 774–780 (2016).
752 69. Kelly, J. R. *et al.* Measuring the activity of BioBrick promoters using an in vivo reference
753 standard. *J. Biol. Eng.* **3**, 4 (2009).
754 70. Zadeh, J. N. *et al.* NUPACK: Analysis and design of nucleic acid systems. *J. Comput.*
755 *Chem.* **32**, 170–173 (2011).
756 71. Hoops, S. *et al.* COPASI—a COmplex PAthway SImulator. *Bioinformatics* **22**, 3067–
757 3074 (2006).
758 72. Madsen Curtis *et al.* Synthetic Biology Open Language Visual (SBOL Visual) Version
759 2.1. *J. Integr. Bioinforma.* (2019) doi:10.1515/jib-2018-0101.
760 73. Der, B. S. *et al.* DNAplotlib: Programmable Visualization of Genetic Designs and
761 Associated Data. *ACS Synth. Biol.* **6**, 1115–1119 (2017).
762 74. Bartoli, V., Dixon, D. O. R. & Gorochowski, T. E. Automated Visualization of Genetic
763 Designs Using DNAplotlib. in *Synthetic Biology: Methods and Protocols* (ed. Braman, J.
764 C.) 399–409 (Springer New York, 2018). doi:10.1007/978-1-4939-7795-6_22.
765 75. Chen, Y.-J. *et al.* Characterization of 582 natural and synthetic terminators and
766 quantification of their design constraints. *Nat. Methods* **10**, 659 (2013).

Figures and captions

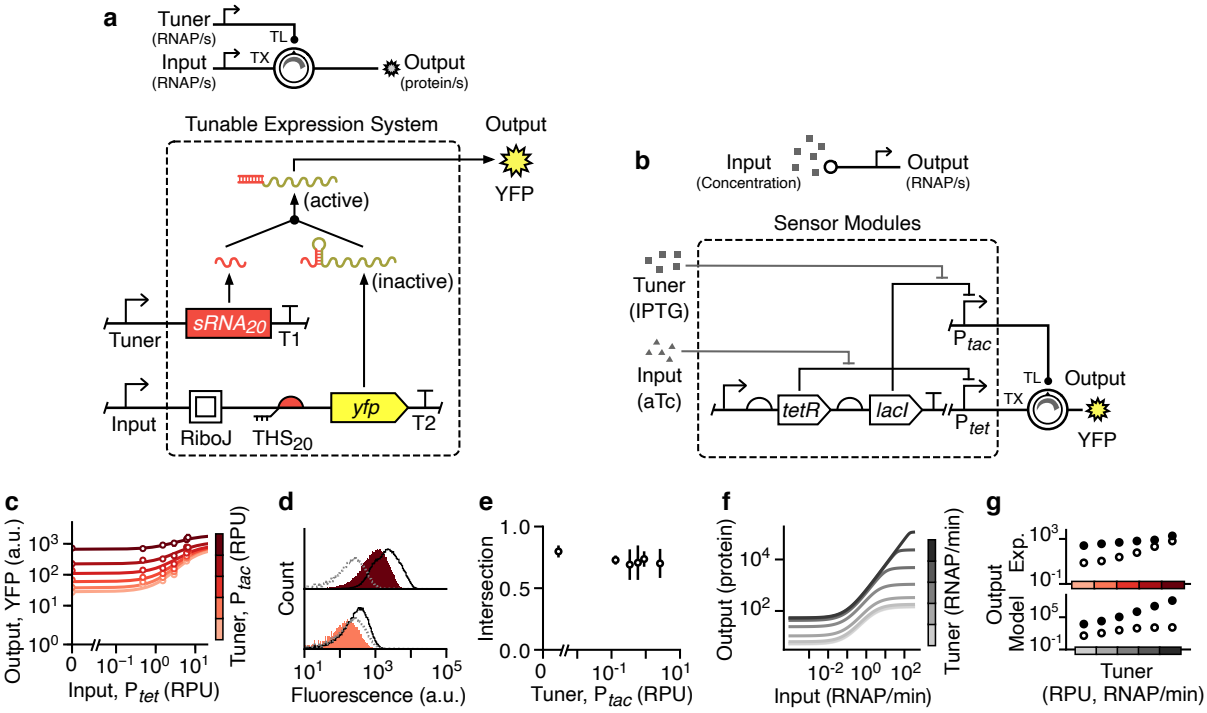

Figure 1: Design and characterization of a tunable expression system (TES). (**a**) Schematic of the TES (top) and genetic implementation using a toehold switch (design 20) [34] to regulate translation (TL) initiation rate of an output protein (bottom, dashed box). Yellow fluorescent protein (YFP) is used as the output and T1 and T2 correspond to the transcriptional terminators L3S3P11 and L3S2P21, respectively [75]. (**b**) Genetic design of the sensor modules used to drive the main and tuner inputs to the TES. (**c**) Experimentally measured response functions for the TES. Points denote the average of three biological replicates and error bars show ±1 standard deviation. Each line shows a fitted Hill function for a fixed tuner input (light–dark: 0.002, 0.03, 0.15, 0.43, 0.9, 2.6 RPU). (**d**) Flow cytometry distributions of output YFP fluorescence when the tuner promoter activity is low (bottom; 0.002 RPU) and high (top; 2.6 RPU). Black outlined distributions correspond to a high input promoter activity (6.6 RPU) and the filled red distributions to a low input promoter activity (0.002 RPU). Cell autofluorescence is shown by the dashed grey line. (**e**) Fraction of intersection between YFP fluorescence distributions for low (0.002 RPU) and high (6.6 RPU) inputs across varying tuner promoter activities. (**f**) Response functions from a deterministic model of the TES (**Supplementary Text S1**). Output shown as the steady state protein level. Line color corresponds to the promoter activity of the tuner input (light–dark: 0.0001, 0.06, 0.3, 1.5, 7.6, 38, 190 RNAP/min). (**g**) Comparison of the output for high (filled circles; 6.6 RPU) and low (unfilled circles; 0.002 RPU) inputs across a range of tuner promoter activities (Experiment: 0.002, 0.03, 0.15, 0.43, 0.9, 2.6 RPU; Model: 0.0001, 0.3, 1.5, 7.6, 38, 190 RNAP/min).

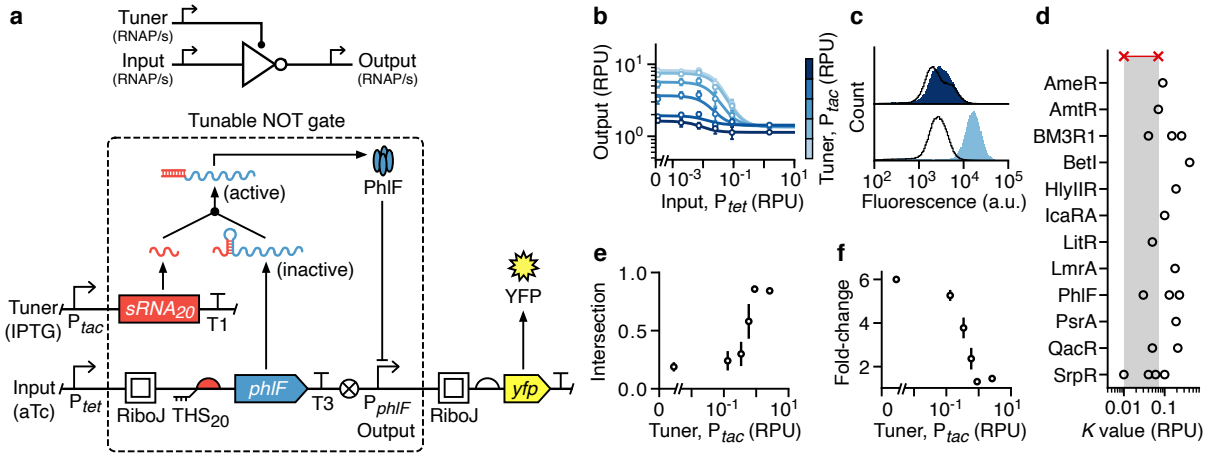

Figure 2: Design and characterization of a tunable NOT gate. (**a**) Schematic of the tunable NOT gate (top) and genetic implementation embedding the TES (bottom, dashed box). Yellow fluorescent protein (YFP) expression is driven by the output promoter and T1 and T3 correspond to the transcriptional terminators L3S3P11 and ECK120033737, respectively [75]. (**b**) Experimentally measured response functions of the tunable NOT gate. Points denote the average of three biological replicates and error bars show ±1 standard deviation. Each line shows a fitted Hill function for a fixed tuner input (light–dark: 0.002, 0.03, 0.15, 0.43, 0.9, 2.6 RPU). (**c**) Flow cytometry distributions of the output YFP fluorescence from the tunable NOT gate when the tuner promoter activity is low (bottom; 0.002 RPU) and high (top; 2.6 RPU). Black outlined distributions correspond to a high input promoter activity (1.5 RPU) and the filled blue distributions to a low input promoter activity (0.002 RPU). (**d**) Comparison of the switching point (*K* value) for each repressor-based NOT gate from Cello [7] (black circles) to the range achievable by the tunable NOT gate (red crosses and shaded regions). (**e**) Fraction of intersection between output YFP fluorescence distributions for low (0.002 RPU) and high (1.5 RPU) inputs across varying tuner promoter activities. (**f**) Fold-change in the median output YFP fluorescence between low (0.002 RPU) and high (1.5 RPU) inputs across varying tuner promoter activities.

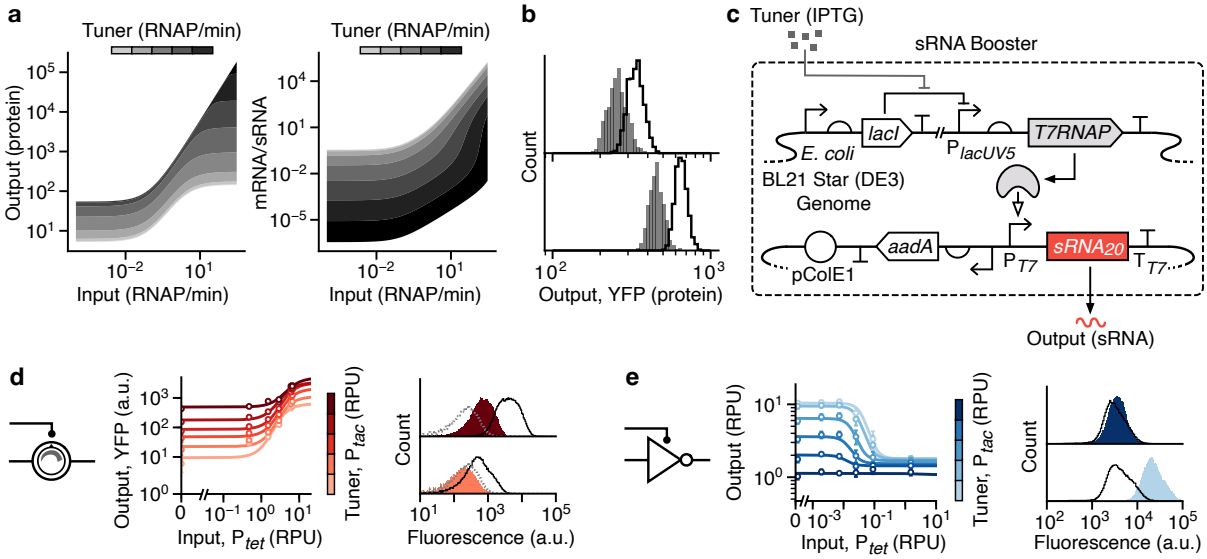

807

808 **Figure 3: Increasing tuner sRNA transcription rate to improve device performance.** (**a**)
809 Results of deterministic simulations of the TES model (**Supplementary Text S1**) showing
810 steady state protein output and THS mRNA to tuner sRNA ratio for a range of input and tuner
811 promoter activities. Tuner promoter activities are shown in bands between (light–dark) 0.0001,
812 0.0005, 0.0024, 0.012, 0.056, 0.27, 1.3, 6.4, 31, 150 and 730 RNAP/min, respectively. (**b**)
813 Stochastic simulation of the TES model (n = 4000) for low (1 RNAP/min; grey) and high (1.5
814 RNAP/min; green) input promoter activity. Top and bottom panels correspond to low (1.5
815 RNAP/min) and high (5 RNAP/min) tuner promoter activities, respectively. (**c**) Genetic design
816 of the sRNA booster. The *T7RNAP* gene is encoded in the host genome and an additional
817 plasmid contains a tuner sRNA expression unit. (**d**) Experimentally measured response
818 functions (left) and flow cytometry distributions of the YFP fluorescence output (right) for the
819 TES with the sRNA booster present. (**e**) Experimentally measured response functions (left)
820 and flow cytometry distributions of the YFP fluorescence output (right) for the tunable NOT
821 gate with the sRNA booster present. Points in all response functions denote the average of
822 three biological replicates and error bars show ±1 standard deviation. Each line shows a fitted
823 Hill function for a fixed tuner input (light–dark: 0.002, 0.03, 0.15, 0.43, 0.9, 2.6 RPU). All flow
824 cytometry distributions are shown for low (bottom; 0.002 RPU) and high (top; 2.6 RPU) tuner
825 promoter activity. Black outlined distributions correspond to a high input promoter activity (6.6
826 RPU for the TES and 1.5 RPU for the NOT gate) and filled red/blue distributions to a low input
827 promoter activity (0.002 RPU). Cell autofluorescence is shown by the dashed grey line.

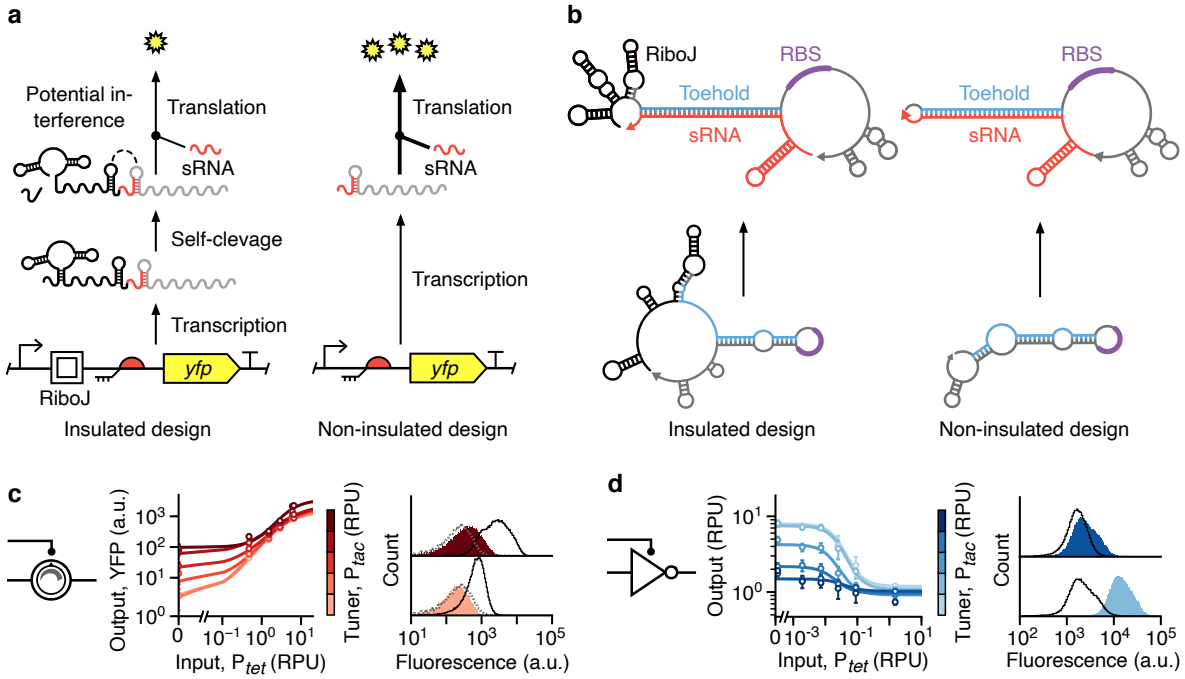

Figure 4: Self-cleaving ribozyme insulators affect tunable device performance. (**a**) Original designs of both the TES and tunable NOT gate include a RiboJ insulating element, which can potentially interfere with binding of the tuner sRNA to the toehold switch. (**b**) RNA secondary structure predictions for THS mRNA alone and with a complimentary tuner sRNA bound. Separate structures shown when the RiboJ insulating element is present (left) and absent (right). (**c**) Experimentally measured response functions (left) and flow cytometry distributions of the output YFP fluorescence (right) for the TES with the RiboJ insulator removed. (**d**) Experimentally measured response functions (left) and flow cytometry distributions of the YFP fluorescence output (right) for the tunable NOT gate with the RiboJ insulator removed. Points in all response functions denote the average of three biological replicates and error bars show ±1 standard deviation. Each line shows a fitted Hill function for a fixed tuner input (light–dark: 0.002, 0.03, 0.15, 0.43, 0.9, 2.6 RPU). All flow cytometry distributions are shown for low (bottom; 0.002 RPU) and high (top; 2.6 RPU) tuner promoter activity. Black outlined distributions correspond to a high input promoter activity (6.6 RPU for the TES and 1.5 RPU for the NOT gate) and filled red/blue distributions to a low input promoter activity (0.002 RPU). Cell autofluorescence is shown by the dashed grey line.

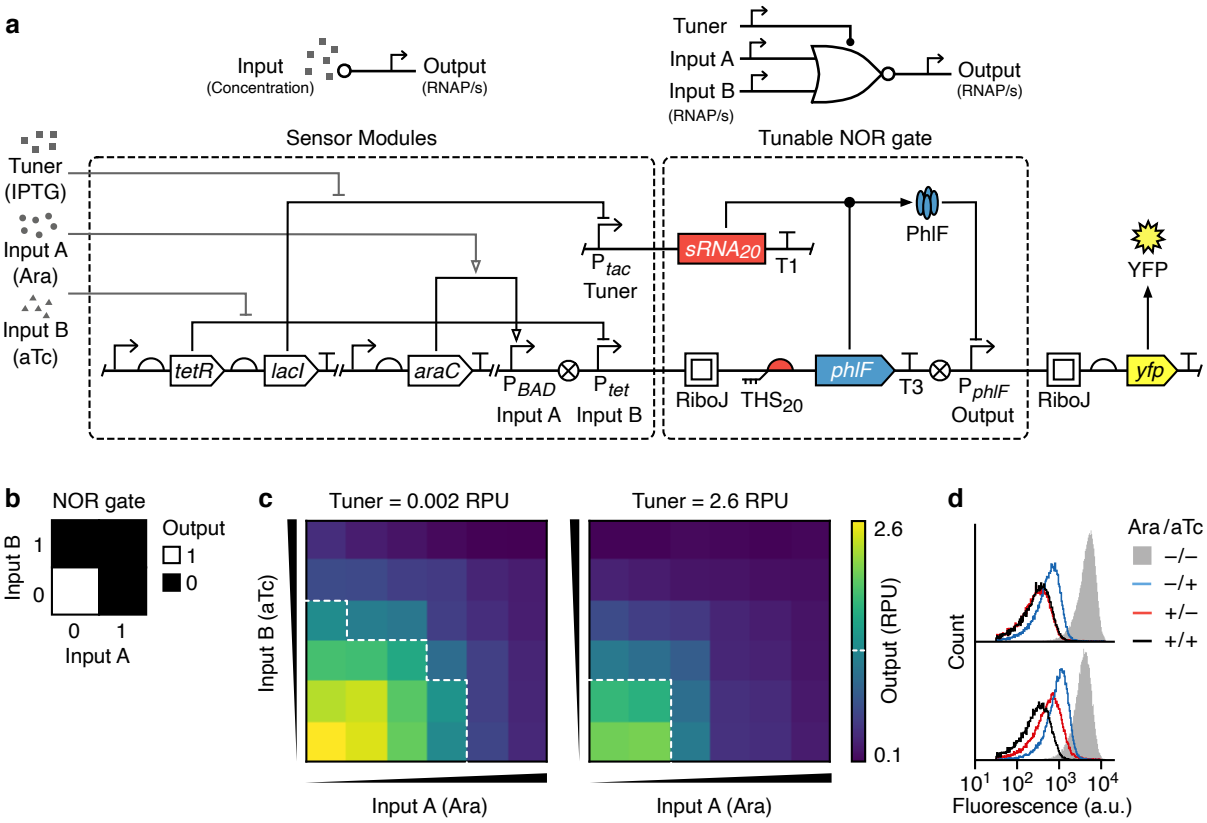

Figure 5: Design and characterization of a tunable NOR gate. (**a**) Schematic of all the sensor systems used (top, left), the tunable NOR gate (top, right), and their genetic implementation (bottom, dashed boxes). Yellow fluorescent protein (YFP) expression is driven by the output promoter and T1 and T3 correspond to the transcriptional terminators L3S3P11 and ECK120033737, respectively [75]. (**b**) Function of a 2-input NOR gate. (**c**) Heatmaps showing the output of the tunable NOR gate for varying input promoter activities (Input A – P_{BAD}: 0.008, 0.003, 0.15, 0.5, 2.5, 3.1 RPU; Input B – P_{tet}: 0.05, 0.5, 1.6, 3.1, 6.4, 7.5 RPU) and for low (left) and high (right) tuner promoter activities. Output promoter activities shown are average values calculated from flow cytometry data for three biological replicates. White dashed line shows an output of 1.2 RPU and denotes the transition point from a high to low output. (**d**) Flow cytometry distributions of the output YFP fluorescence for tuner promoter activities of 0.002 RPU (bottom) and 2.6 RPU (top). The four distributions correspond to combinations of the absence and presence of L-Arabinose (10 mM) and aTc (50 ng/mL).

860 ## Tables

861 **Table 1: Performance summary of TES and tunable NOT gate.**

Device	Design	Dynamic range[a,b] (a.u.)		Fold-change[a,c]		Intersection[a,d]		*K* range (RPU)[g]
		Low[e]	High[f]	Low[e]	High[f]	Low[e]	High[f]	
TES	Original	333 ± 53	877 ± 695	14 ± 1.7	2.4 ± 1.2	0.78 ± 0.06	0.69 ± 0.16	–
	sRNA booster[h]	538 ± 51	2064 ± 1070	227 ± 297	5.7 ± 1.8	0.46 ± 0.04	0.35 ± 0.15	–
	Non-insulated[i]	882 ± 134	2149 ± 409	445 ± 412	31 ± 16	0.26 ± 0.07	0.27 ± 0.06	–
	Combined[j]	1550 ± 209	1712 ± 584	1236 ± 613	66 ± 54	0.15 ± 0.04	0.22 ± 0.04	–
NOT gate	Original	17280 ± 1273	3512 ± 286	6.0 ± 0.1	1.5 ± 0.1	0.19 ± 0.04	0.84 ± 0.02	0.01–0.07
	sRNA booster[h]	22040 ± 1601	2170 ± 654	5.8 ± 0.3	0.9 ± 0.3	0.13 ± 0.07	0.85 ± 0.02	0.01–0.06
	Non-insulated[i]	17466 ± 1926	4061 ± 827	6.8 ± 0.3	2.6 ± 0.4	0.11 ± 0.03	0.56 ± 0.08	0.02–0.04
	Combined[j]	27751 ± 3104	2383 ± 165	6.0 ± 0.6	0.9 ± 0.1	0.08 ± 0.05	0.90 ± 0.03	0.003–0.02

862 a. Average values are shown ± 1 standard deviation calculated from flow cytometry data for three
863 biological replicates.
864 b. Dynamic range calculated as the absolute difference in YFP fluorescence between low and high
865 inputs (0.002 and 6.6 RPU for the TES, and 0.002 and 1.5 RPU for the NOT gate, respectively).
866 c. Fold-change in YFP fluorescence (corrected for cell autofluorescence) for low and high inputs
867 (0.002 and 6.6 RPU for the TES, and 0.002 and 1.5 RPU for the NOT gate, respectively).
868 d. Fraction of intersection between the flow cytometry YFP fluorescence distributions for low and high
869 inputs (0.002 and 6.6 RPU for the TES, and 0.002 and 1.5 RPU for the NOT gate, respectively)
870 (**Materials and Methods**).
871 e. Performance measured for a low tuner input (0.002 RPU). This is the expected promoter activity of
872 the P_{tac} promoter in our designs.
873 f. Performance measured for a high tuner input (2.61 RPU). This is the expected promoter activity of
874 the P_{tac} promoter in our designs.
875 g. Range of *K* values from Hill functions fitted to experimental data.
876 h. Original designs (**Figures 1a** and **2a**) with the sRNA booster system (**Figure 3c**).
877 i. Design has the RiboJ insulating element removed (**Figure 4a**).
878 j. Design has the RiboJ insulating element removed (**Figure 4a**), and sRNA booster system present
879 (**Figure 3c**).